# Making corrections to your proof

Please follow these instructions to mark changes or add notes to your proof. You can use Adobe Acrobat Reader (download the most recent version from **https://get.adobe.com**) or an open source PDF annotator.

The tools you need to use are contained in **Annotations** in the **Comment** toolbar. You can also right-click on the text for several options. The most useful tools have been highlighted here. If you cannot make the desired change with the tools, please insert a sticky note describing the correction.

Please ensure all changes are visible via the 'Comments List' in the annotated PDF so that your corrections are not missed.


Attach file
Highlight text
Insert sticky note
Insert text
Replace text
Strikethrough text
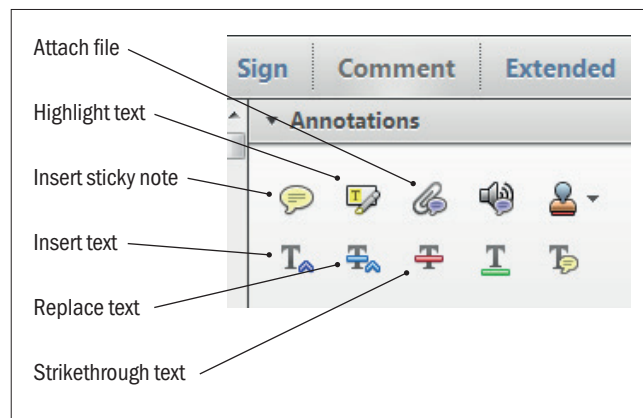
Do not attempt to directly edit the PDF file as changes will not be visible.

Replacing text

To replace text, highlight what you want to change then press the replace text icon, or right-click and press 'Add Note to Replace Text', then insert your text in the pop up box. Highlight the text and right click to style in bold, italic, superscript or subscript.
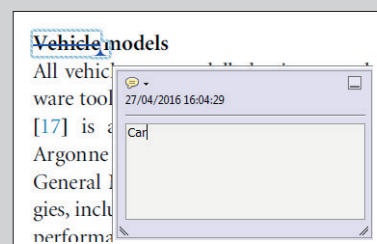

Inserting text

Place your cursor where you want to insert text, then press the insert text icon, or right-click and press 'Insert Text at Cursor', then insert your text in the pop up box. Highlight the text and right click to style in bold, italic, superscript or subscript.
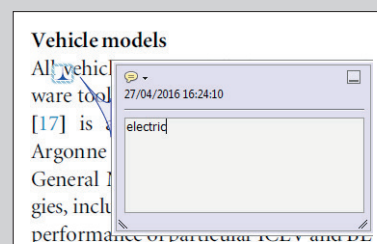
### Deleting text

To delete text, highlight what you want to remove then press the strikethrough icon, or right-click and press 'Strikethrough Text'.
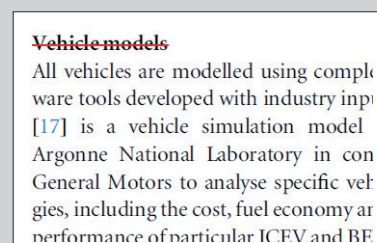
Highlighting text

To highlight text, with the cursor highlight the selected text then press the highlight text icon, or right-click and press 'Highlight text'. If you double click on this highlighted text you can add a comment.
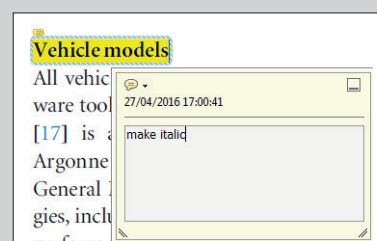
QUERY FORM

SMALL CAPS JOURNAL: The Astronomical Journal

AUTHOR: Bouma et al.

TITLE: PTFO 8-8695: Two Stars, Two Signals, No Planet

ARTICLE ID: ajab9e73

Your article has been processed in line with the journal style. Your changes will be reviewed by the Production Editor, and any amendments that do not comply with journal style or grammatical correctness will not be applied and will not appear in the published article.

The layout of this article has not yet been finalized. This proof may contain columns that are not fully balanced/matched or other typographical imperfections; these issues will be resolved once the final corrections have been incorporated.

Please check that the **names of all authors as displayed in the proof are correct**, and that all **authors are linked to the correct affiliations**. Please also confirm that the correct corresponding author has been indicated. **Note that this is your last opportunity to review and amend this information before your article is published**.

If you have an Acknowledgments section, please check that the information there is complete and correct and that all relevant institutions, grant numbers, programs, and collaborators are mentioned as appropriate.

We have been provided with ORCID iDs for the authors as below. Please confirm whether the numbers are correct.
L. G. Bouma 0000-0002-0514-5538
J. N. Winn 0000-0002-4265-047X
G. R. Ricker 0000-0003-2058-6662
R. Vanderspek 0000-0001-6763-6562
D. W. Latham 0000-0001-9911-7388
S. Seager 0000-0002-6892-6948
J. M. Jenkins 0000-0002-4715-9460
T. Barclay 0000-0001-7139-2724
K. A. Collins 0000-0001-6588-9574
D. R. Louie 0000-0002-2457-272X
S. N. Quinn 0000-0002-8964-8377
M. E. Rose 0000-0003-4724-745X
J. C. Smith 0000-0002-6148-7903
B. Wohler 0000-0002-5402-9613

Page 6

Q1
Please define the acronym MAST.

Page 14

Q2
Please check the details for any journal references that do not have a link; please update with correct details and supply a CrossRef DOI or NASA ADS link if available.

Page

Q3
Please update if possible all references where only the arXiv preprint number is given.

Q4

Please provide the version details of software in references [Bhatti et al. 2018, Brasseur et al. 2019, Lightkurve Collaboration et al. 2018].

Q5

Please provide the title of the code for the [Brasseur et al. 2019] reference.

Q6

Please provide the publisher details in reference [Briceño et al. 2007b, Bryson et al. 2020, Foreman-Mackey2016, Millan-Gabet et al. 2007, Winn 2010].

Q7

In the references [Burnham & Anderson 2016, Donati et al. 2016, Onitsuka et al. 2017, Vogt et al. 1994], please provide volume or page number, as needed.

Q8

Please update references [Foreman-Mackey et al. 2020, Ginsburg et al. 2018, Jones et al. 2001, Rebull et al. 2020, Salvatier et al. 2016, Servén et al. 2018] if possible.

Q9

Please provide conference details in reference [McKinney 2010]. The format for conference citations is [Publication, Conference title, editors (Publisher City, State: Publisher Name), page number].

CrossMark

PTFO 8-8695: Two Stars, Two Signals, No Planet

L. G. Bouma[1] , J. N. Winn[1] , G. R. Ricker[2] , R. Vanderspek[2] , D. W. Latham[3] , S. Seager[2,4,5] , J. M. Jenkins[6] ,
T. Barclay[7,8] , K. A. Collins[3] , J. P. Doty[9], D. R. Louie[10] , S. N. Quinn[3] , M. E. Rose[6] , J. C. Smith[6,11] ,
J. Villaseñor[2], and B. Wohler[6,11]

[1] Department of Astrophysical Sciences, Princeton University, 4 Ivy Lane, Princeton, NJ 08540, USA; luke@astro.princeton.edu
[2] Department of Physics and Kavli Institute for Astrophysics and Space Research, Massachusetts Institute of Technology, Cambridge, MA 02139, USA
[3] Center for Astrophysics | Harvard & Smithsonian, 60 Garden St, Cambridge, MA 02138, USA
[4] Department of Earth, Atmospheric and Planetary Sciences, Massachusetts Institute of Technology, Cambridge, MA 02139, USA
[5] Department of Aeronautics and Astronautics, MIT, 77 Massachusetts Avenue, Cambridge, MA 02139, USA
[6] NASA Ames Research Center, Moffett Field, CA 94035, USA
[7] NASA Goddard Space Flight Center, 8800 Greenbelt Road, Greenbelt, MD 20771, USA
[8] University of Maryland, Baltimore County, 1000 Hilltop Circle, Baltimore, MD 21250, USA
[9] Noqsi Aerospace Ltd., 15 Blanchard Avenue, Billerica, MA, 01821, USA
[10] Department of Astronomy, University of Maryland, College Park, MD 20742, USA
[11] SETI Institute, Mountain View, CA 94043, USA

Abstract

PTFO 8-8695 (CVSO 30) is a star in the 7–10 million year old Orion OB1a cluster that shows brightness dips that resemble planetary transits. Although strong evidence against the planet hypothesis has been presented, the possibility remains debated in the literature. To obtain further clues, we inspected data from the NASA Transiting Exoplanet Survey Satellite (TESS) and the ESA Gaia mission. The Gaia data suggest that PTFO 8-8695 is a binary: the photometric data show it to be overluminous with respect to members of its kinematic group, and the astrometric data are inconsistent with a single star. The TESS light curve shows two different photometric periods. The variability is dominated by a sinusoidal signal with a period of 11.98 hr, presumably caused by stellar rotation. Also present is a 10.76 hr signal consisting of a not-quite sinusoid interrupted by hour-long dips, the type of signal previously interpreted as planetary transits. The phase of the dips is nearly 180° away from the phase of the originally reported dips. As noted previously, this makes them difficult to explain as planetary transits. Instead, we believe that PTFO 8-8695 is a pair of young and rapidly rotating M dwarfs, one of which shows the same "transient-dipper" behavior that has been seen in at least five other cases. The origin of these transient dips is still unknown but likely involves circumstellar material.

Unified Astronomy Thesaurus concepts: Exoplanet evolution (491); Pre-main-sequence stars (1290); Stellar rotation (1629); Variable stars (1761); Low mass stars (2050)

1. Introduction

We wish PTFO 8-8695b were a planet. It would be quite exceptional. It would be the youngest known transiting[12] hot Jupiter (van Eyken et al. 2012), orbiting a T Tauri star in the Orion OB1a cluster. It would have the shortest orbital period of any hot Jupiter. With such a short period, it would probably be filling its Roche lobe and actively losing mass to its host star. Not only that, but the rapidly rotating host star is probably oblate enough to cause the planet's orbit to precess into and out of the transiting configuration on a timescale of years (Barnes et al. 2013; Ciardi et al. 2015; Kamiaka et al. 2015).

Another first would be the direct detection of Hα emission from a close-in planet (Johns-Krull et al. 2016). In addition to the chromospheric Hα emission, it seems that there is an additional Hα emission with radial velocity (RV) variations in phase with the planetary orbit. The average velocity width of the excess Hα emission is 87 km s^{-1}, and its equivalent width is 70%–80% that of the stellar chromosphere (Johns-Krull et al. 2016). The proposed explanation is that the emission is from hot material flowing away from the planet (Johns-Krull et al. 2016).

However, the observed signals have some peculiarities that make the planet seem even more unusual, to the point that they cast into doubt the premise that PTFO 8-8695b is real. First, the transit-like brightness dips are about three times deeper in optical bandpasses (e.g., g-band) than in the near-infrared (e.g., z-band; Onitsuka et al. 2017; Tanimoto et al. 2020). An ordinary atmosphere expected for a Jovian planet would not lead to such a strong color dependence of the transits. Second, the planet does not seem to emit as much infrared radiation as would be expected for such a hot Jovian planet (Yu et al. 2015). Third, despite measurement attempts by multiple investigators, PTFO 8-8695b does not seem to show the Rossiter effect at the amplitude expected given the rapid stellar rotation and large planet size (Ciardi et al. 2015; Yu et al. 2015). Fourth, the phase of the dips within the overall period of photometric variability has changed drastically over the years since their initial discovery. To counter these objections, it has been proposed that the planet may be much smaller than Jupiter and that the dips are produced by dust clouds emitted from the planet (Tanimoto et al. 2020).

A separate issue is that the brightness dips change shape over many orbital cycles. This was initially explained by Barnes et al. (2013) as the natural effects of gravity darkening. However, Howarth (2016) argued that the necessary amplitude of gravity darkening is too large to be realistic, given the

---

[12] Two younger hot Jupiters have been reported around V830 Tau and TAP 26 (Donati et al. 2016, 2017; Yu et al. 2017).

spectroscopically determined rotation velocity. Additionally, as the gravity-darkened star precesses about its rotation axis, it would show photometric variability that has not been observed.

While the planetary interpretation clearly faces challenges, there is no completely satisfactory alternate explanation. Low-latitude starspots, hot or cold, would struggle to produce photometric features as short as some of the observed dips. High-latitude accretion hot spots might produce the observed Hα variability but require fine-tuning to produce dips of the appropriate duration. Transits by dust clumps or other dusty features are questionable because PTFO 8-8695 does not have a detectable infrared (IR) excess associated with the presence of warm dust (e.g., Yu et al. 2015, Figure 18). In addition, the sublimation times for dust grains of plausible composition could be quite short (Zhan et al. 2019).

A relevant fact is that between 0.1% and 1% of rapidly rotating low-mass stars in $\mathcal{O}(10)$ Myr old associations show short-duration dips as part of their overall periodic variability (Rebull et al. 2018). The dips can persist over months, but their depths often vary and sometimes change immediately after stellar flares. The explanation proposed by Stauffer et al. (2017) and David et al. (2017) to explain this novel class of variable stars is that a clumpy torus of dust and gas orbits near the Keplerian corotation radius. To this point, though, it has not been clear if this explanation applies to PTFO 8-8695, because the determination of the stellar rotation period has been somewhat ambiguous (van Eyken et al. 2012; Koen 2015; Raetz et al. 2016).

We begin in Section 2 by describing newly available observations from NASA's Transiting Exoplanet Survey Satellite (TESS; Ricker et al. 2015) and ESA's Gaia (Gaia Collaboration et al. 2018). The TESS light curve shows two different periodic signals, which we analyze in Section 3. The Gaia data, analyzed in Section 4, show that PTFO 8-8695 is too bright to be a single star and also suggest it is an astrometric binary. We discuss the pieces of the puzzle in Section 5, and we summarize the situation in Section 6. In a postscript, we comment on a recent study by Koen (2020) that reached similar conclusions.

2. The Data

2.1. TESS Observations

PTFO 8-8695 (also known as CVSO 30; Briceño et al. 2005) was observed by TESS with Camera 1, CCD 1, from 2018 December 15 until 2019 January 6, during the sixth sector of science operations (Ricker et al. 2015). The star is designated TIC 264461976 in the TESS Input Catalog (Stassun et al. 2018, 2019). The pixel data for an 11×11 array surrounding PTFO 8-8695 were averaged into 2 minute stacks by the onboard computer. Each 2048×2048 image from the CCD was also averaged into 30 minute stacks and saved as a "full frame image" (FFI).

The 2 minute stacks for PTFO 8-8695 were reduced to light curves by the Science Processing Operations Center (SPOC) at the NASA Ames Research Center (Jenkins et al. 2016). We mainly used the Presearch Data Conditioning Simple Aperture Photometry (PDCSAP) light curve. The PDC light curve is based on pixels chosen to maximize the signal-to-noise ratio of the total flux of the target (Bryson et al. 2020). Nonastrophysical variability was removed by fitting out trends common to many stars (Smith et al. 2012; Stumpe et al. 2014).

As an independent check on the 2 minute SPOC light curve, we examined the light curve based upon 30 minute image stacks that was produced as part of the Cluster Difference Imaging Photometric Survey (CDIPS; Bouma et al. 2019). Our CDIPS light curve of choice used a circular aperture with radius 1 pixel.

To clean the data, we removed all points with nonzero quality flags, which indicate known problems (e.g., Tenenbaum & Jenkins 2018). We also masked out the data from the first and last 6 hr of each orbit because there are often systematic effects in the photometry during those times. Both the CDIPS and PDC light curves showed a discontinuous jump in the last few days of orbit 20, which seemed likely to be an instrumental systematic effect and led us to mask out the data with time stamps ranging from BJD 2458488.3 until the end of the orbit. The PDC light curve initially had 15,678 points. The quality-flag cut removed 854 points, masking the orbit edges removed an additional 716 points, and removing the data from the final few days of orbit 20 removed an additional 1079 points. After cleaning, 83% of the initial flux measurements remained.

We normalized the light curve by dividing out the median flux, and we then opted to subtract 1.0 to set the median value to zero, which simplified subsequent interpretation. Many of these and subsequent processing steps were performed using `astrobase` (Bhatti et al. 2018).

2.2. Gaia Observations

2.2.1. Astrometric Measurements

Between 2014 July 25 and 2016 May 23, Gaia measured about 300 billion centroid positions of 1.6 billion stars (Gaia Collaboration et al. 2016, 2018; Lindegren et al. 2018). For the Gaia second data release (DR2), these CCD observations were used to determine positions, proper motions, and parallaxes of the brightest 1.3 billion stars (Lindegren et al. 2018). For PTFO 8-8695, there were 121 "good" observations, that is, observations that were not strongly down-weighted in the astrometric solution. PTFO 8-8695 was assigned the Gaia DR2 identifier 3222255959210123904. Its brightness was measured using selected bands (G, Rp, and Bp) of the Gaia Radial Velocity Spectrometer (Cropper et al. 2018; Evans et al. 2018). We accessed the pipeline parameters for PTFO 8-8695 using the Gaia archive.[13]

The majority of Gaia's derived parameters for PTFO 8-8695 agree with expectations based on previous studies (Briceño et al. 2005; van Eyken et al. 2012). The main novelty is that Gaia DR2 reported a 10.3σ "astrometric excess," indicating that the residuals to the best-fitting astrometric model were larger than expected based on the statistical uncertainties. We comment on the significance and interpretation of this excess in Section 4.

2.2.2. Hierarchical Cluster Membership

Gaia also provided astrometric parameters for tens of thousands of young stars in the Orion complex. Stellar populations in giant molecular cloud complexes are not monolithic; substructured groups are the norm (Briceño et al. 2007b). The Orion molecular cloud complex in particular has numerous subgroups, with ages ranging from 0.5 to 15 Myr.

---

[13] gea.esac.esa.int/archive/

See, for instance, Briceño et al. (2005, 2007a), Jeffries et al. (2006), Kounkel et al. (2018), and Briceño et al. (2019).

PTFO 8-8695 was initially designated CVSO 30 and identified as a member of the Orion OB1a subassociation by Briceño et al. (2005), based on photometry and spectroscopy. Later work by Briceño et al. (2007a) clarified that PTFO 8-8695 is in a kinematically distinct subgroup of Orion OB1a, named the "25 Ori" group after its brightest member. They reported that the 25 Ori group has an isochrone age of 7–10 Myr and a smaller fraction of stars with disks than younger nearby subassociations (Hernández et al. 2007).

With the Gaia astrometry, it has become clear that 25 Ori itself has distinct subgroups (Kounkel et al. 2018; Briceño et al. 2019). In describing the cluster membership of PTFO 8-8695, we follow the notation and results of Kounkel et al. (2018). These authors combined astrometric data from Gaia DR2 with near-infrared spectra from APOGEE-2 (Gunn et al. 2006; Blanton et al. 2017; Majewski et al. 2017; Zasowski et al. 2017; Cottle et al. 2018). They performed a hierarchical clustering on the six-dimensional position and velocity information to identify subgroups within the Orion complex. From smallest to largest, PTFO 8-8695 was identified as a member of the following hierarchical subgroups:

$$25 \text{ Ori} - 1 \subset 25 \text{ Ori} \subset \text{Orion OB1a} \subset \text{Orion D}, \qquad (1)$$

where "$\subset$" means "is a proper subset of." 25 Ori-1 is the largest subgroup of 25 Ori, with 149 identified members. The mean age of the 25 Ori-1 subgroup, determined by fitting isochrones to group members with APOGEE effective temperatures and Gaia parallaxes, was determined to be 8.5 ± 1.2 Myr (see Kounkel et al. 2018, Section 2.3). Kounkel et al. (2018) also identified seven smaller groups in the Orion complex near the Be star 25 Ori. These groups received sequential identifiers, for example, 25 Ori-2 (age = 12.9 ± 2.8 Myr; see also Briceño et al. 2019).

While all members of the Orion complex are young relative to the field, these considerations are essential for assessing photometric evidence for the binarity of PTFO 8-8695 because of the degeneracy between stellar luminosity and age for pre-main-sequence stars. Having a clean sample of reference stars that are tightly associated with PTFO 8-8695—both spatially and kinematically—minimizes contamination not only from field stars, but also from older and younger members of the Orion complex.

3. TESS Analysis

3.1. Inspection

Our initial inspection of the TESS light curve, in both its 2 minute PDCSAP and 30 minute FFI forms, showed a strong sinusoidal beat signal (Figures 1 and 2, top panel). As a precursor to more detailed analysis, we calculated generalized Lomb–Scargle periodograms using `astrobase` (Lomb 1976; Scargle 1982; VanderPlas & Ivezić 2015; Bhatti et al. 2018). The tallest peak occurs at 11.98 hr, and a second strong peak occurs at 10.76 hr. We will refer to these two periods as the "longer period" P_ℓ and the "shorter period" P_s. Lower-power harmonics of both signals are also present.

The peak-to-peak maximum amplitude of the light curve, when the two signals interfere constructively, is about 14%. During the times of destructive interference, the peak-to-peak amplitude is about 6%. Assuming the signals are mainly

sinusoidal, simple algebra tells us that the peak-to-peak amplitudes should be about 10% for the longer-period signal and 4% for the shorter-period signal. To view the phase-folded light curves of the longer-period signal, we subtracted the best-fitting sinusoid with a period equal to P_s. The resulting light curve appears smooth and nearly sinusoidal. But after subtracting the best-fitting sinusoid with a period equal to P_ℓ, visual inspection of the phase-folded light curve revealed a substructure resembling the "dips" seen in previous observations. In particular, there was an $\approx 1\%$ dip lasting about an hour. These initial impressions turned out to be consistent with the results of our more complicated analysis, described below.

3.2. Light Curve Model

We fitted a model to the light curve consisting of a linear combination of Fourier modes with periods P_s and P_ℓ, as well as a number of harmonics chosen as described below. To try to account for the dips, we also added an analytic transit model with period P_s. Symbolically, the total flux f is given as

$$f = f_s + f_\ell = f_{\text{transit,s}} + f_{\text{Fourier,s}} + f_{\text{Fourier},\ell}, \qquad (2)$$

where f_s is the flux at the shorter period, and f_ℓ is the flux at the longer period. Writing out the Fourier terms explicitly, we have

$$f = f_{\text{transit,s}} + \sum_{n=1}^{N_s} A_n \sin(n\omega_s t) + \sum_{n=1}^{N_s} B_n \cos(n\omega_s t)$$
$$+ \sum_{m=1}^{N_\ell} A_m \sin(m[\omega_\ell t + \phi_\ell]) + \sum_{m=1}^{N_\ell} B_m \cos(m[\omega_\ell t + \phi_\ell]),$$
$$(3)$$

where N_s and N_ℓ are the total number of modes at the shorter and longer periods, respectively; A_i and B_i are the amplitudes of each mode (which can be positive or negative); and ω_ℓ and ω_s are the angular frequencies of the longer-period and shorter-period signals. By not including a phase parameter in the shorter-period model, we have implicitly defined the zero-point of the phase scale. The relative phase of the longer-period model is specified by the phase parameter ϕ_ℓ. Since we did not know in advance how many harmonics would be appropriate to include in the model, we considered a number of different choices for N_s and N_ℓ, and we used the Bayesian information criterion (BIC) to select the final model (Table 1).

The free parameters are as follows. The transit model parameters are the impact parameter, the planet-to-star radius ratio, two quadratic limb-darkening parameters, the planet's orbital period (set equal to P_s), the time of a particular transit, and the mean flux. We sampled the stellar radius and mass from prior probability distributions, implicitly defining the stellar density, which (together with the orbital period) sets the transit timescale. There are also the parameters defining the Fourier modes. As an example, one possible model consists of a transit, $N_s = 2$ sines and cosines at the shorter period, plus $N_\ell = 1$ sine and cosine at the longer period. There are $2N_s = 4$ additional Fourier amplitudes at the shorter period, plus $2N_\ell = 2$ Fourier amplitudes at the longer period, as well as P_ℓ itself and the relative phase ϕ_ℓ. The total number of parameters is 17 for this case.

We implemented and fitted the models using `PyMC3`, which is built on `theano` (Salvatier et al. 2016; Theano Development Team 2016). For the Fourier terms, we used the default
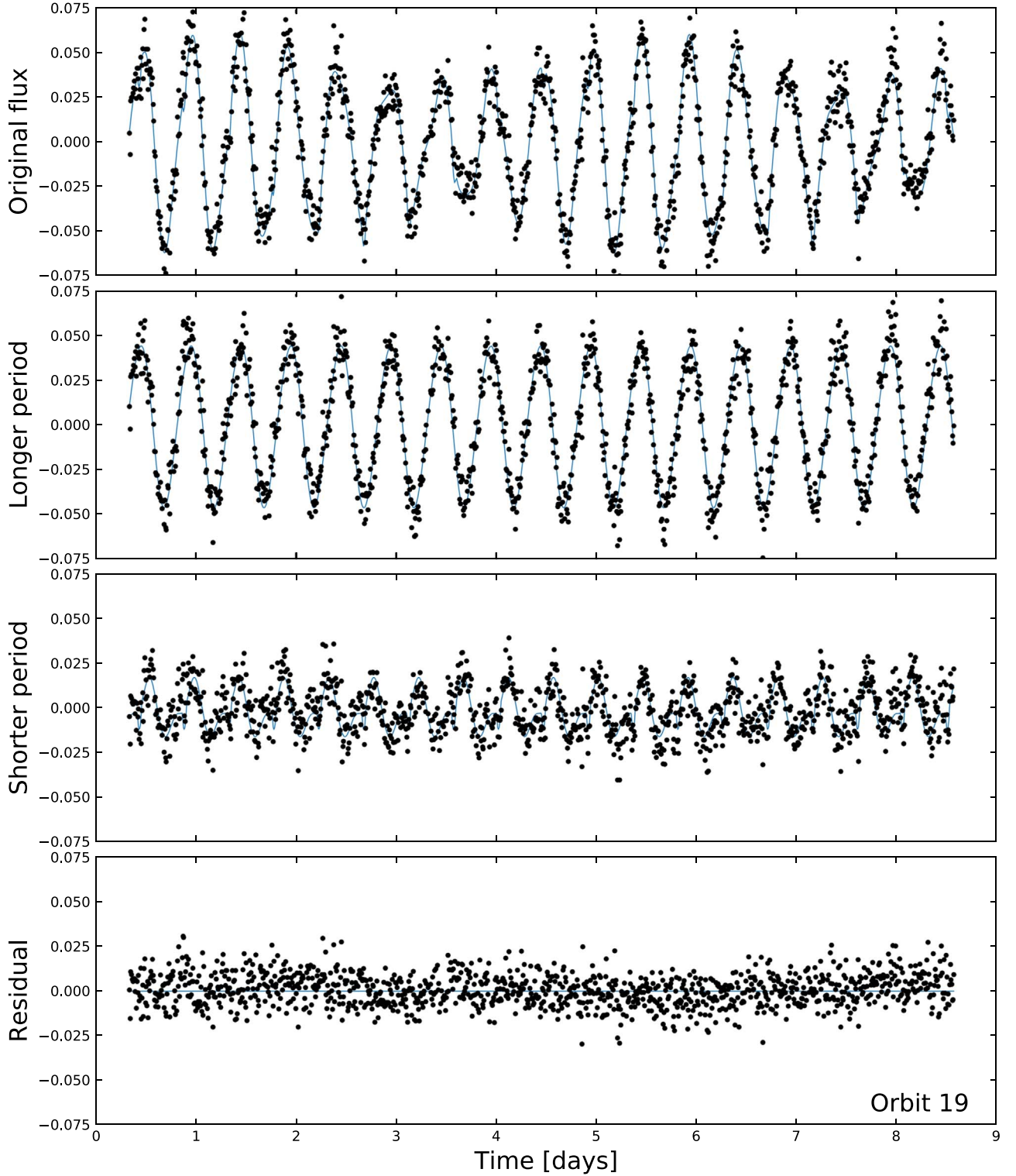
Figure 1. TESS light curve of PTFO 8-8695 (Sector 6, Orbit 19). Top: original (PDCSAP median-subtracted) relative flux. The beat period of 4.48 days is visible by eye. The blue curve is a model including two harmonics at the longer period P_ℓ, plus three harmonics and a transit at the shorter period P_s. Upper middle: longer-period signal, equal to the original signal minus the shorter-period signal. Lower middle: shorter-period signal, equal to the original signal minus the longer-period signal. Bottom: residual relative flux. The data are binned from 2 to 10 minute cadence for convenience in plotting and fitting.

math operators. For the exoplanet transit, we used the model and derivatives implemented in the exoplanet code (Fore-man-Mackey et al. 2020). Our priors are listed in Table 2. To speed up the fitting process, we averaged the 2 minute light curve into 10 minute samples. We correspondingly scaled down the uncertainties in the flux measurements by a factor of

$\sqrt{5}$. Before sampling, we initialized each model with the parameters of the maximum a posteriori (MAP) model. We then assumed a Gaussian likelihood and sampled using PyMC3's gradient-based No-U-Turn Sampler (Hoffman & Gelman 2014), and we used $\hat{R}$ as our convergence diagnostic (Gelman & Rubin 1992). We tested our ability to successfully
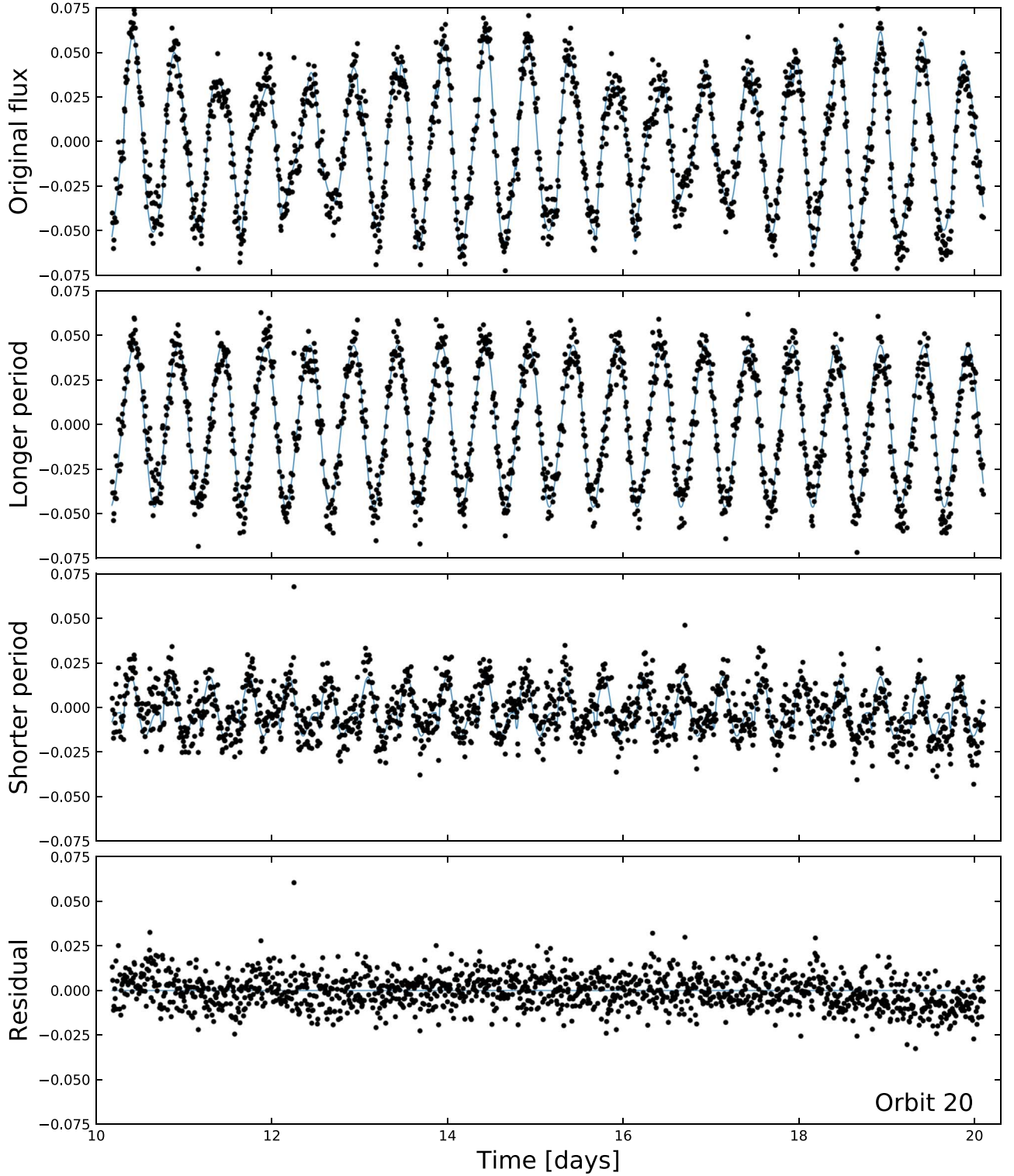
Figure 2. TESS light curve of PTFO 8-8695 (Sector 6, Orbit 20). Same format as Figure 1.

recover injected parameters using synthetic data before fitting the PTFO 8-8695 light curves.

3.3. Fitting Results

We considered nine models, with the number of modes per frequency (N_s and N_ℓ) ranging from one to three. To select our preferred model, we used the Bayesian information criterion (Table 1). The model with the lowest BIC had three modes at

the shorter 10.76 hr period and two modes at the longer 11.98 hr period. The other models had BIC values that implied significantly less support (Burnham & Anderson 2016). All nine models have reduced χ^2 values ranging between 1.21 and 1.68, which suggest a plausible though imperfect agreement between the data and the model to within the formal uncertainties. Table 2 gives the best-fitting parameters for the preferred model, which has the lowest BIC value.

Table 1
Model Comparison

Description	N_s	N_ℓ	N_{data}	N_{param}	χ^2	χ^2_{red}	BIC	ΔBIC
Favored	3	2	2585	21	3102.4	1.210	3267.4	0.0
Disfavored	2	3	2585	21	3179.0	1.240	3344.0	76.6
…	2	2	2585	19	3237.4	1.262	3386.7	119.3
…	3	3	2585	23	3217.1	1.256	3397.9	130.4
…	2	1	2585	17	3312.6	1.290	3446.1	178.7
…	3	1	2585	19	3397.5	1.324	3546.8	279.4
…	1	2	2585	17	4101.2	1.597	4234.8	967.3
…	1	3	2585	19	4160.8	1.622	4310.1	1042.7
…	1	1	2585	15	4318.4	1.680	4436.2	1168.8

Note. N_s and N_ℓ are the number of harmonics at the short and long periods, respectively. N_{data} is the number of fitted flux measurements. N_{param} is the number of free parameters in the model. The Bayesian information criterion and the difference from the maximum ΔBIC are also listed.

To explore where each model succeeded and failed, we split the original signal into its respective components (Figures 1 and 2). We also examined the phase-folded signals (Figure 3).

In every model, the 11.98 hr variability is a simple sinusoid with peak-to-peak amplitude ≈10%. The 10.76 hr variability is always more complex. The overall impression is of a distorted sinusoidal function, with a peak-to-peak amplitude of about 4%. The asymmetric sinusoid rises to a maximum near phase 0.25 and reaches minimum brightness between phases −0.5 and −0.25. Between phases −0.5 and 0.0, there appears to be a complex shorter-timescale variability, ending with a "dip" of depth ≈1.2%, lasting ≈0.75 hr. The fact that our preferred model has three rather than two "short period" harmonics is linked to the degree of curvature required between phases −0.5 and −0.05: the analog $(N_\ell, N_s) = (2, 2)$ model prefers a longer transit duration but does not fit the out-of-transit curvature as well, particularly immediately before ingress.

The periodogram of the residuals between the data and the preferred model shows a barely significant and poorly resolved peak at ≈8 days, consistent with the visual impression of some slower trends in the bottom rows of Figures 1 and 2.

4. Tests for Binarity

4.1. Visual Binarity

The portion of the sky subtended by each TESS pixel is about 21″ on a side. Before making any interpretations, we needed to consider whether light from neighboring stars could have contributed to the photometric signal we are attributing to PTFO 8-8695. The scene is shown in Figure 4. In the upper panels, the pixels used to measure the background level in the SPOC light curve are indicated with "X" hatching, and the pixels used in the final light-curve aperture are shown with "/" hatching.

The target star, PTFO 8-8695 (TIC 264461976), has a T-band magnitude of 14.0, and its position is shown with a star. The other (unlabeled) star inside the target aperture, TIC 264461979, has $T = 16.8$ and so cannot contribute more than about 10% to the total signal. The only other known star that is sufficiently close and bright that its light might contaminate the signal from the target star is TIC 264461980, with $T = 14.8$. This star, which we dub "Star A," is 23″6 northwest of the target. Based on the magnitude difference, Star A could

contribute flux variations as large as 48% of the flux of the target star.

The variability of PTFO 8-8695 with a period consistent with P_s had already been observed based on images with arcsecond resolution. Thus, our main concern regarding blending was whether the longer-period signal with period P_ℓ originated from PTFO 8-8695 or from Star A. We took two approaches to investigate the source of the long-period signal.

First, we examined the CDIPS FFI light curves of the target, which are available on MAST (Bouma et al. 2019). Three light curves are available, based on photometric apertures with a radius of 1, 1.5, or 2.5 pixels. The maximal peak-to-peak beat amplitude was the same to within a percent, regardless of the size of the photometric aperture that was used to create the light curve. If Star A were the source of the long-period variability, we would expect the peak variability amplitude to be smallest in the 1 pixel aperture, based on the separation of the sources (Figure 4, bottom). From this test alone, it seems unlikely that Star A is the source of the long-period signal. [Q1]

Second, we examined the 2 minute light curve of each individual pixel in the scene, using the interactive tools implemented in lightkurve (Lightkurve Collaboration et al. 2018). If Star A were the source of the long-period variability, we would expect the pixels nearest to Star A to show a sinusoidal signal with amplitude exceeding 10%. The data do not show this pattern. The data from the pixel directly below Star A does not show any sinusoidal variability; the peak-to-peak variability seen in that pixel is ≲8%. In contrast, the southeastern-most pixel within the PTFO 8-8695 aperture (the pixel farthest from Star A that was used in the optimal aperture) shows the longer-period sinusoidal variability signal with an amplitude of 14%. We conclude that within the resolution of the Gaia DR2 source catalog, the P_s and P_ℓ signals originate from PTFO 8-8695. Based on the work of Ziegler et al. (2018), we can surmise that stellar companions with separations wider than ≈1″ (349 au) and within $\Delta G \approx 3$ mag of PTFO 8-8695 would have likely been detected through this approach.

Stronger constraints on possible stellar companions were obtained by van Eyken et al. (2012) through high-resolution imaging with the NIRC2 camera on the Keck II 10 m telescope. They reported 3σ H-band magnitude difference limits of 4.3, 6.4, and 8.9 at angular separations of 0″25, 0″5, and 1″0 (87, 175, and 349 au). They also detected a point source 7.0 mag fainter than the target and 1″8 to the northeast (which is not included in the Gaia

Table 2
Best-fit Model Priors and Posteriors

Param.	Unit	Prior	Mean	Std. Dev.	3rd Pct.	97th Pct.
Sampled						
P_s	days	$\mathcal{N}(0.4485; 0.0010)$	0.4484613	0.0000460	0.4483731	0.4485416
$t_s^{(1)}$	days	$\mathcal{N}(0.438096; 0.0020)$	0.4388368	0.0011286	0.4367929	0.4410297
$R_p/R_\star$	...	$\mathcal{N}(0.1100; 0.0110)$	0.11171	0.00679	0.09950	0.12437
b	...	$\mathcal{U}(0; 1 + R_p/R_\star)$	0.8205	0.0523	0.7188	0.9071
u_1	...	(2)	0.693	0.501	0.	1.638
u_2	...	(2)	-0.01	0.429	-0.804	0.806
Mean	...	$\mathcal{U}(-0.01; 0.01)$	-0.001019	0.000185	-0.001365	-0.000669
$R_\star$	$R_\odot$	$\mathcal{T}(1.23; 0.40)$	1.20	0.40	0.44	1.90
$M_\star$	$M_\odot$	$\mathcal{T}(0.39; 0.25)$	0.42	0.22	0.	0.78
$A_{s,0}$	...	$\mathcal{U}(-0.02; 0.02)$	0.009083	0.000371	0.008396	0.009763
$B_{s,0}$	...	$\mathcal{U}(-0.02; 0.02)$	0.009696	0.000391	0.008914	0.010352
$A_{s,1}$	...	$\mathcal{U}(-0.02; 0.02)$	0.001646	0.000351	0.000990	0.002297
$B_{s,1}$	...	$\mathcal{U}(-0.02; 0.02)$	-0.005456	0.000307	-0.005998	-0.004861
$A_{s,2}$	...	$\mathcal{U}(-0.02; 0.02)$	0.000177	0.000252	-0.000295	0.000655
$B_{s,2}$	...	$\mathcal{U}(-0.02; 0.02)$	-0.000581	0.000271	-0.001110	-0.0001
ϕ_ℓ	rad	$\mathcal{U}(1.3721; 2.1575)$	1.80542	0.20468	1.47712	2.09634
ω_ℓ	rad days^{-1}	$\mathcal{N}(12.6054; 0.1261)$	12.588753	0.000972	12.586968	12.590517
$A_{\ell,0}$	...	$\mathcal{U}(-0.06; 0.06)$	0.03929	0.004331	0.031501	0.045035
$B_{\ell,0}$	...	$\mathcal{U}(-0.06; 0.06)$	0.019891	0.008161	0.0071	0.032232
$A_{\ell,1}$	...	$\mathcal{U}(-0.02; 0.02)$	0.002189	0.000516	0.001203	0.003021
$B_{\ell,1}$	...	$\mathcal{U}(-0.02; 0.02)$	-0.002311	0.000496	-0.003063	-0.001364
Derived						
ω_s	rad days^{-1}	...	14.01054	0.00144	14.00803	14.01330
R_p	R_{Jup}	...	1.30	0.44	0.53	2.16
$a/R_\star$	...	...	1.81	3.17	0.35	3.29

Note. $\mathcal{U}$ denotes a uniform distribution, $\mathcal{N}$ a normal distribution, and $\mathcal{T}$ a truncated normal bounded between zero and an upper limit much larger than the mean. Note that $R_p/R_\star$ has been corrected for the dilution by Star A and other neighboring stars, according to the PDCSAP light curve's CROWDSAP value (0.73) in the optimal aperture. (1) To convert mean TESS midtransit time to BJD$_{TDB}$, add 2,458,468.2. (2) Quadratic limb-darkening prior from Kipping (2013), implemented by Foreman-Mackey et al. (2020).

DR2 catalog). Due to its relative faintness, this object cannot be the source of the shorter- and longer-period TESS signals.[14]

4.2. Photometric Binarity

We also used the Gaia data to see if the observed luminosity of PTFO 8-8695 is too high to be from a single star, that is, if the object is a "photometric binary." To assemble a set of stars coeval with PTFO 8-8695, we used the 25 Ori-1 members identified by Kounkel et al. (2018) and discussed in Section 2.2.2. To define a set of nonmember stars that nonetheless are subject to similar selection criteria, we defined the reference "neighborhood" as the group of at most 10^4 randomly selected nonmember stars within five standard deviations of the mean values of the R.A., decl., and parallax of 25 Ori-1. We queried Gaia DR2 for these stars using astroquery (Ginsburg et al. 2018). This yielded 1819 neighbors. While some of these stars may indeed be members of the Orion complex, or even of 25 Ori-1, enforcing this cut on positions and parallaxes ensures that we are comparing stars with similar amounts of interstellar reddening.

We examined the resulting five-dimensional distribution of R.A., decl., proper motion in both directions and parallax. The

first point we noted was that 25 Ori-1 is a clearly defined overdensity in each dimension: the cluster was confirmed to exist and to be distinct from the neighborhood. The second point we noted is that PTFO 8-8695 belongs to the cluster, based on its properties in each of these dimensions.

Figure 5 shows the H-R diagram we constructed from the data. The diagram shows that PTFO 8-8695 is ≈0.75 mag brighter than the average 25 Ori-1 star of the same color. In other words, it is about twice as bright as expected for a single star in the cluster. It also seems to be part of a "photometric binary" track that runs above and parallel to the main track.

The implication is that either (1) PTFO 8-8695 is notably younger than the kinematically identical 25 Ori-1 members or (2) PTFO 8-8695 is a binary with two components of nearly equal brightness. Because there is no other reason to suspect an age difference, and because the source showed two separate photometric signals with similar but distinct periods, the binary interpretation seems more probable.

4.3. Astrometric Binarity

A separate line of evidence for binarity is the Gaia DR2 astrometry. As noted in Section 2, the Gaia DR2 astrometric solution for PTFO 8-8695 shows a 10.3σ "astrometric excess," a parameter that quantifies the degree to which a single-star model fails to fit the astrometric measurements. Specifically, the single-source astrometric model yielded $\chi^2 = 325.2$. There

---

[14] This point source was claimed to be a potential planetary-mass object (Schmidt et al. 2016). Subsequent analysis of its colors showed that it is a background star (Lee & Chiang 2018).
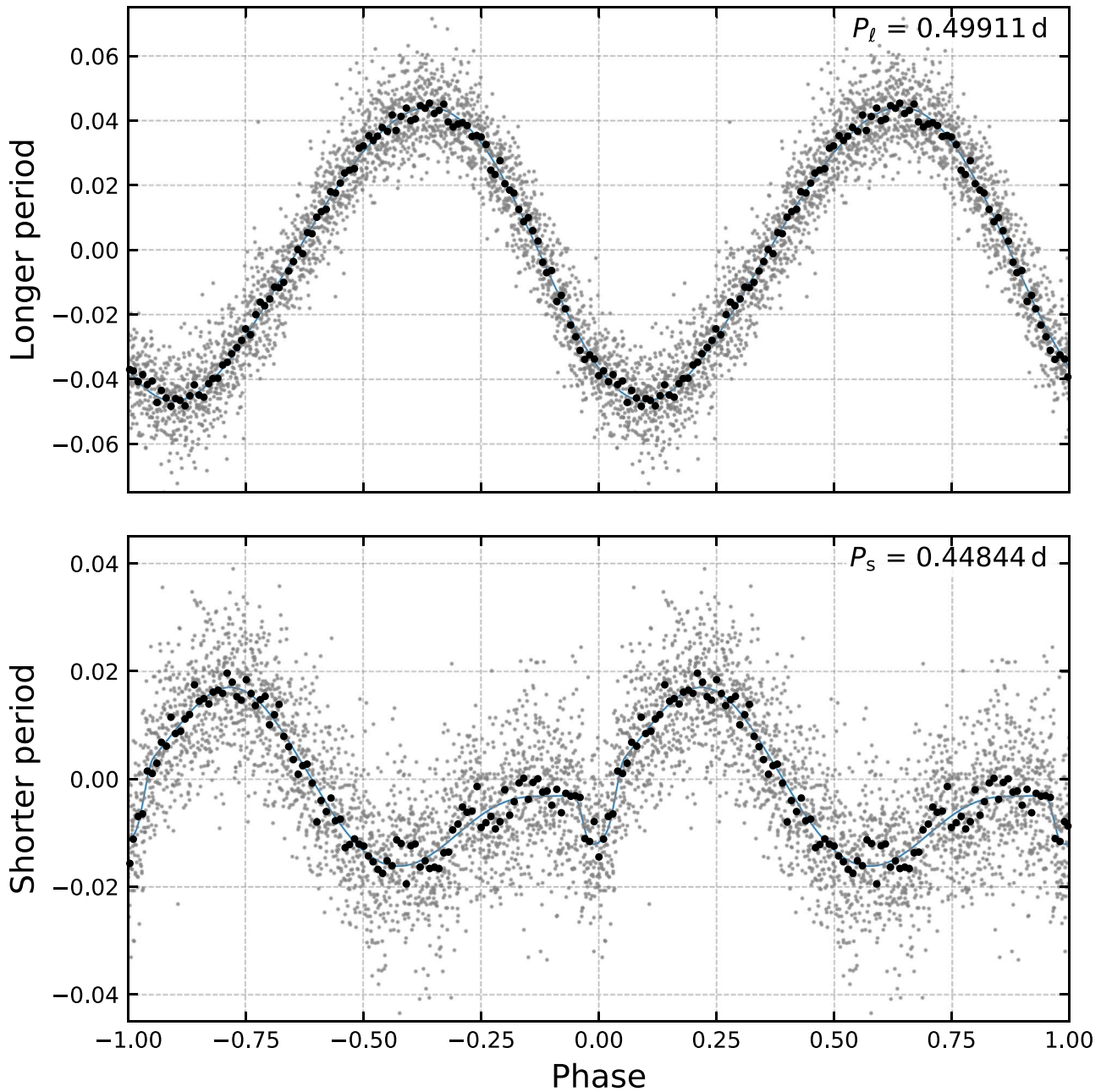
Figure 3. Phase-folded longer- and shorter-period signals. Top: longer-period signal. Bottom: shorter-period signal. The phase is defined such that the dip occurs at zero phase. Gray points are the `PDCSAP` data binned to 10 minute cadence. Black points are binned to 100 points per period. The model (blue line) includes two harmonics at the longer period and three harmonics and a transit at the shorter period.

are 121 astrometric measurements and five free parameters, and therefore 116 degrees of freedom. The reduced χ^2 is 2.80. While the majority of stars with comparable brightness in Gaia do not show such poor goodness-of-fit, many M dwarfs do, because of a color-dependent term in the mission's point-spread function model (see Lindegren et al. 2018, Appendix A). The reduced χ^2 has been "renormalized" to account for this, yielding a modified statistic called the renormalized unit weight error (RUWE[15]).

We acquired the RUWE for each of the 149 members in 25 Ori-1 identified by Kounkel et al. (2018). We then queried the CDIPS light curve database at MAST (Bouma et al. 2019)

to find the subset of members that were at least as variable as PTFO 8-8695. We measured the variability amplitude by taking the difference between the 95th and 5th percentiles of the flux measurements. This yielded 30 stars of equal or greater variability. The lower panel of Figure 5 shows the RUWE of these stars as a function of stellar brightness. PTFO 8-8695 is at the 93rd percentile of equally variable stars within the 25 Ori-1 group. Two of the 30 stars with variability amplitudes greater than 9.7% showed higher RUWE. One was CVSO 35, which has a TESS light curve that varies by 2 mag and shows both a strong Wide-field Infrared Survey Explorer (WISE, Wright et al. 2010) IR excess and also a 10 μm silicate emission feature (Maucó et al. 2018). The other star was GAIA DR2 3222210363837122048.
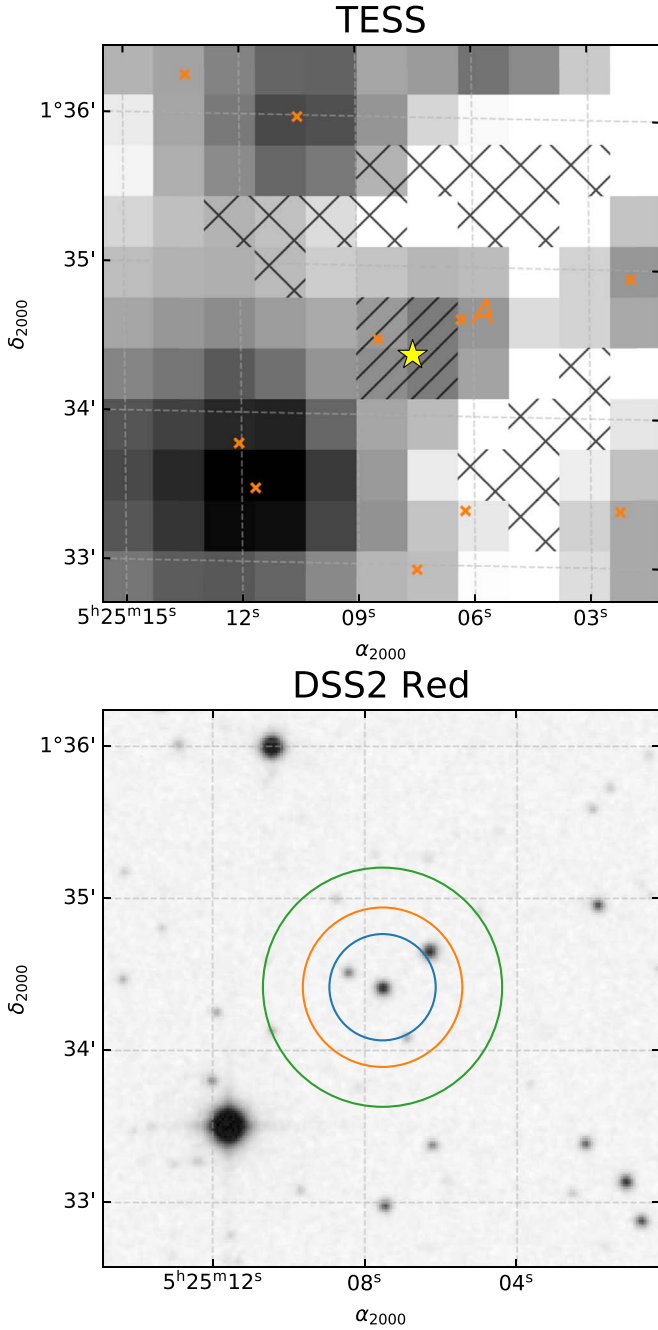
TESS

DSS2 Red

Figure 4. Scene used for blend analysis. Top: mean TESS image of PTFO 8-8695 over Sector 6, with a logarithmic gray scale. The yellow star is the position of PTFO 8-8695. Orange crosses are neighboring stars with $T < 17$. The X and / hatches show the apertures used to measure the background and target star flux, respectively. Bottom: digitized Sky Survey R-band image of the same field, with a linear gray scale. The circles show the apertures of radii 1, 1.5, and 2.25 pixels used in our blend analysis. To the northwest of PTFO 8-8695 and between the blue and orange circles is "Star A," the only star bright and close enough to be contributing to the signal attributed to PTFO 8-8695. However, the pixel-level TESS data showed that Star A is not the source of the observed variability (see Section 4.1).

Potential explanations for an elevated RUWE include photometric variability and unresolved stellar binarity (e.g., Rizzuto et al. 2018; Belokurov et al. 2020). If photometric variability were the root cause, we would expect stars with similar brightness and color in the same kinematic group of Orion to show similar astrometric excesses, because the
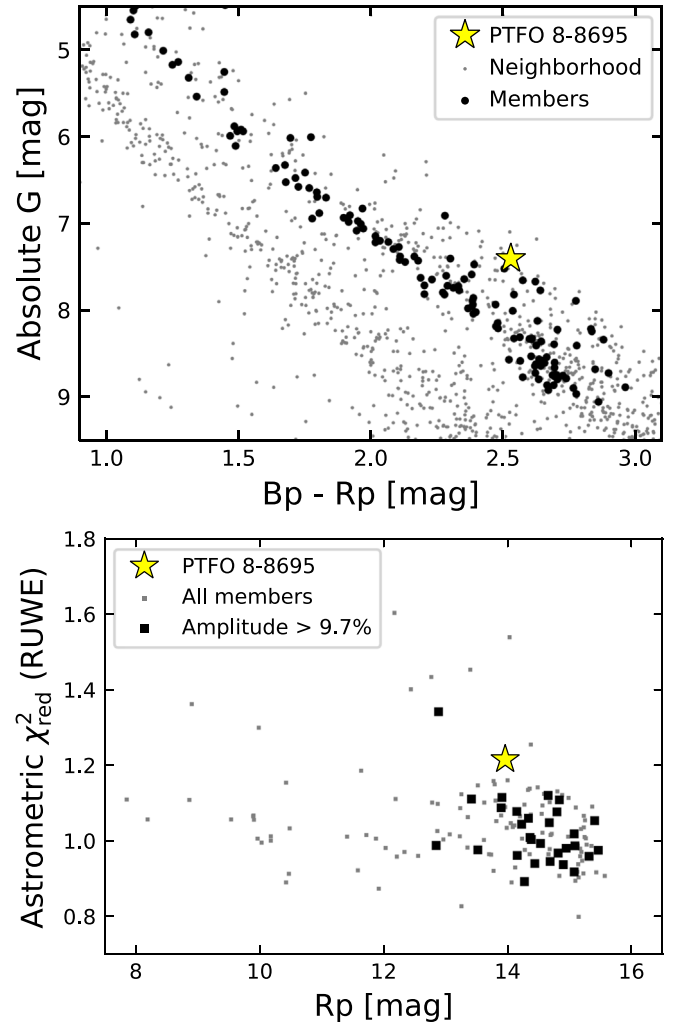
Figure 5. Evidence for binarity in PTFO 8-8695. Top: Hertzsprung–Russell diagram of PTFO 8-8695 and late-type members of 25 Ori-1. Black circles are members of the 25 Ori-1 group identified by Kounkel et al. (2018). Gray circles are stars in the "neighborhood," that is, nonmember stars for which the R.A., decl., and parallax are within five standard deviations of the mean values for 25 Ori-1. The neighborhood contains members of the Orion complex with its full spread of ages, in addition to field interlopers. G denotes the Gaia broadband magnitude, Bp Gaia blue, Rp Gaia red, and ω_{as} the parallax in arcseconds. The x-axis limits are chosen to display only the K and M dwarfs, accentuating PTFO 8-8695's separation from the single-star sequence. Bottom: renormalized astrometric unit weight error (RUWE) vs. Rp magnitude for 25 Ori-1 members. The single-source astrometric model for PTFO 8-8695 provides a poor fit to the data, which could be due to either stellar variability or binarity. But since cluster members that are at least as variable as PTFO 8-8695 show lower astrometric excesses (black squares), binarity is the likely reason.

majority of young stars are highly variable. However, relative to other M dwarf group members with comparable brightnesses and variability characteristics, PTFO 8-8695 still stands out by virtue of its failure to conform to a single-star astrometric model. This supports the interpretation that PTFO 8-8695 is a binary star.

We will have to wait for the next data release of the Gaia mission for a more definitive determination of whether the astrometric excess is caused by stellar binarity or photometric variability. Nonetheless, the fact that comparably variable stars do not show comparably large astrometric excesses suggests that stellar binarity is indeed the root cause.

4.4. RV Binarity

RV measurements over sufficiently long timescales could also reveal the presence of multiple stars in this system. Unfortunately, the available RV data for PTFO 8-8695 are sparse, presumably due to the difficulties of performing RV observations of such a faint and rapidly rotating star. The RV data sets with the longest time baselines we could find in the literature were those reported by van Eyken et al. (2012). These included five Keck/HIRES measurements acquired over 10 days in 2011 April, and four HET/HRS measurements acquired over 10 days in 2011 February. The rms RV over each 10 day span was $\approx 2\,\mathrm{km\,s^{-1}}$, consistent with the measurement precision. Although van Eyken et al. (2012) tried a CCF-based RV reduction technique, they eventually found that manually selecting absorption lines and measuring line centroids were more effective. While Yu et al. (2015) acquired 22 further Keck/HIRES spectra over one night in 2013 December, those points were not reduced to velocities. Further RV observations could potentially confirm or refute the presence of binary companions.

5. Discussion

5.1. Longer-period Signal

The standard interpretation for 11.98 hr nearly sinusoidal modulations of a pre-main-sequence M dwarf is stellar rotation. This is the dominant signal in the system with 10% amplitude, and there is no evidence to suggest that this signal has any other origin.

In their report on the discovery of the unusual photometric variability, van Eyken et al. (2012) saw an alias of the longer-period signal (e.g., their Figure 7) in the form of a peak in the periodogram at 23.96 ± 0.15 hr. They ascribed it to their observing cadence because of its close correspondence to the sidereal day. Our pixel-level analysis showed that the signal is specific to only pixels near PTFO 8-8695 and no other pixels. We therefore conclude that the signal is not an artifact of systematic errors.

We are not the first to reach the conclusion that the long-period sinusoidal modulation is astrophysical. Koen (2015) identified the same modes and aliases as van Eyken et al. (2012) and argued that the signal was astrophysical, even if the exact period was still unclear. Using photometry from the YETI global telescope network, Raetz et al. (2016) came to the conclusion that the 11.98 hr signal was indeed from stellar rotation. The TESS data strongly support this conclusion.

5.2. Shorter-period Signal, Including the "Dip"

The TESS light curve shows a dip that lasts about 45 minutes and recurs every 10.76 hr (Figures 1–3). The dip duration is roughly the same as that observed by previous investigators (van Eyken et al. 2012; Yu et al. 2015). The 1.2% depth is similar to what has been observed in the near-infrared (Onitsuka et al. 2017). However, the dip depth seems likely to have evolved over time, between being not present at all and a maximum of $\approx 5\%$ (e.g., Koen 2015; Yu et al. 2015; Tanimoto et al. 2020).

An interesting feature of the sequence of dips is that the phase of the dips has been observed to change with time (Yu et al. 2015). In fact, Tanimoto et al. (2020) provided stark
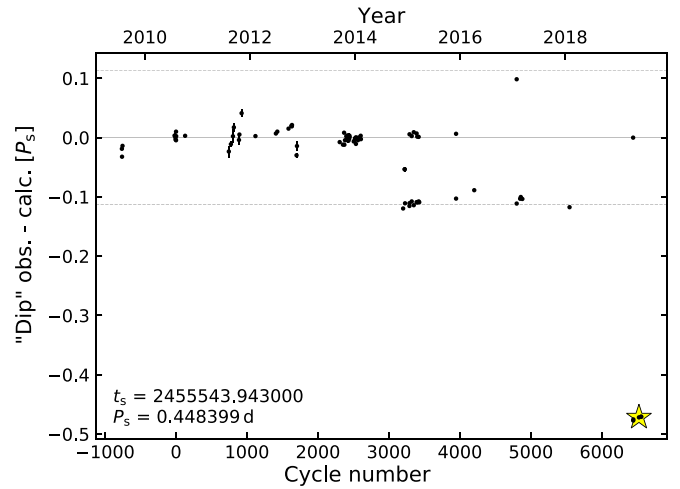

Figure 6. Timing residuals for PTFO 8-8695b based on a decade of monitoring. Black points are times of dips, minus the indicated linear ephemeris. The phase of the shorter-period signal is plotted on the y-axis. The star symbol represents the TESS ephemeris. Dips were observed by van Eyken et al. (2012), Ciardi et al. (2015), Yu et al. (2015), Raetz et al. (2016), Onitsuka et al. (2017), and Tanimoto et al. (2020). Certain dips (e.g., the one at phase 0 in mid-2019) are consistent with noise and were likely reported because dips were expected, rather than convincingly observed. Horizontal dashed lines are drawn at $\pm(P_\ell - P_s)/P_s$, highlighting a possible numerical coincidence. The orbital phase observed by TESS (lower right) is consistent with that of Tanimoto et al. (2020).

evidence for a different behavior altogether: over a time span of years, the dip "split" into distinct groups at particular phases. See, for instance, their Figures 2 through 4. Fitting a decade of observations, they provided the following constant-period ephemeris, which we did not find any need to update:

$$t_0\ \mathrm{BJD_{TDB}} = 2455543.943 \pm 0.002$$
$$P = 0.4483993 \pm 0.0000006 \text{ days.} \qquad (4)$$

Figure 6 shows the differences between the observed "midtransit" times of the dips and the times calculated using Equation (4). The phase of the dips seen by TESS (yellow star) agrees with the independent 2018 December measurements by Tanimoto et al. (2020): either the dip abruptly shifted phase over the past decade or, more likely, there are multiple dips that have come and gone at different phases.

Figure 6 shows two additional strange features: (1) multiple dips per cycle and (2) a set of dips at a phase that is numerically coincident with $(P_\ell - P_s)/P_s$. The observation of multiple dips per cycle in 2015 was seen independently by both Yu et al. (2015) and Tanimoto et al. (2020). It therefore seems credible. Inspecting the Tanimoto et al. (2020) light curves, we find that the claim of multiple dips per cycle in 2018 December at phase 0 and −0.47 seems less plausible. The dips at phase −0.47 are strongly detected, while the suggested dip at phase 0 is not clearly detected.

We are not sure what to make of the numerical coincidence. The ratio of long to short periods is roughly 10:9. It is not clear that this would obviously translate into an observational bias unless, by some fluke, three season's worth of observations managed to only observe every ninth dip. This is of course not the case, and we therefore leave this curiosity as observation *sans* interpretation.

5.3. *Short-period Modulation outside Dips*

Visually, the out-of-dip modulation at the 10.76 hr period resembles a slightly asymmetric sinusoid (Figure 3). The best model has nonzero amplitudes for both the first and second harmonics (Table 2). The third harmonic is formally present with marginal ($\approx 2\sigma$) significance. The first sine and cosine harmonics both have amplitudes of roughly $0.90\% \pm 0.04\%$. The second sine harmonic has amplitude $0.16\% \pm 0.04\%$, so it is nonzero at a significance of $\approx 4\sigma$. The second cosine harmonic has an amplitude of $-0.55\% \pm 0.03\%$. In our sign convention, the fact that it is negative means that this component peaks at phase 0.25 and 0.75, that is, the quadratures of the orbit.

5.3.1. *Ellipsoidal Variability?*

If there were a giant planet transiting PTFO 8-8695, it would tidally distort the host star and cause ellipsoidal photometric modulations that peak at the quadratures (see Shporer 2017). Interpreting the second cosine harmonic as planet-induced tidal distortion would imply a minimum planet mass $M_{\rm p} \sin i$ of $3.8\,M_{\rm Jup}$. For this estimate, we assumed $R_\star = 1.39 R_\odot$ and $M_\star = 0.39 M_\odot$ (van Eyken et al. 2012). This ellipsoidal amplitude is larger than the typical modulations induced by close-in giant planets because the host star is puffy and still on the pre-main-sequence.

The planetary interpretation, however, does not readily explain the large first sine and cosine harmonics. Interpreting the sine component as Doppler beaming would imply a secondary mass greater than the primary ($0.86\,M_\odot$). Interpreting the cosine component as reflected or emitted light from the planet's surface is nonsensical because the sign is wrong: the planet would need to be *absorbing* light.

5.3.2. *Similar Light Curves*

When physical explanations are not forthcoming, we often resort to taxonomy. By searching the literature, we found about a dozen light curves with morphologies similar to PTFO 8-8695, drawn from surveys of low-mass, weak-lined T Tauri stars in regions including ρ Oph, Upper Sco, Taurus, and perhaps the Pleiades (Parks et al. 2014; Rebull et al. 2016, 2018, 2020; David et al. 2017; Stauffer et al. 2017, 2018). The clearest matches came from K2 (Howell et al. 2014), but a few analogs were potentially also found using 2MASS (YLW 1C and YLW 10C; Parks et al. 2014) and CoRoT (Stauffer et al. 2015). We downloaded a subset of the K2 light curves from MAST, opting for the EVEREST reductions (Luger et al. 2016, 2018). They are plotted in Figure 7.

These light curves have been phenomenologically classified as "persistent flux dips" or "transient flux dips," based on whether their depths and durations show variability over the 90 day K2 campaigns (Stauffer et al. 2017). In the terminology of Stauffer et al. (2017), these objects are morphologically distinct from "scallop shell" light curves and are present in stars at more advanced evolutionary disk stages than the "dipper" stars (Ansdell et al. 2016; Bodman et al. 2017; Cody & Hillenbrand 2018). The persistent and transient flux dip stars all show angular dips that cannot be explained as the effects of starspots. These stars typically have the following things in common:

1. They are weak-lined T Tauri stars (under the definition of, e.g., Fang et al. 2009).
2. The spectral type is M2 to M5 (e.g., Rebull et al. 2018, Figure 20).
3. The age is typically $\lesssim 100\,{\rm Myr}$.[16]
4. The light curves show shallow, angular dips, superposed on large-amplitude smooth variability at or near 1:1 synchronicity. The smooth variability is interpreted as stellar rotation.
5. The rotation is rapid, with a period that is usually between 0.5 and 2.0 days.
6. There is rarely any infrared excess that is detectable in the WISE data (never any W4 detection; only a few W3 detections).
7. They sometimes show multiple dips per cycle.
8. The dip depths, durations, and phases can vary over just a few cycles (e.g., EPIC 204143627).
9. The dip depths can change after flares.
10. They are rare at a population level, with an occurrence rate between 0.1% and 1% of young M2–M5 stars (Rebull et al. 2018).

The 10.76 hr signal in PTFO 8-8695 meets all of these criteria. While this was mentioned by Stauffer et al. (2017), the asymmetric out-of-dip modulation shown by the TESS data solidifies the connection.

There are two crucial additional points concerning the transient flux dips. First, the dip durations seem to scale linearly with the photometric periods (Stauffer et al. 2017, Figure 26). In contrast, the transit duration T of a small obstructing object across the stellar disk scales as $T \propto R_\star\,(P/M_\star)^{1/3}$ (Winn 2010). While the shortest-period ≈ 0.5 day transient flux dip stars have dip durations consistent with point sources, at longer periods of 1–5 days the dip durations become many hours, which is too long to be caused by planetary transits.

Second, approximately 40%–50% of the transient flux dip stars discovered in ρ Oph and Upper Sco show two Lomb–Scargle periods, a possible sign of binarity (Stauffer et al. 2017, Table 1). This is higher than the main-sequence companion fraction of $\mathrm{CF}^{\rm MS}_{0.1-0.5 M_\odot} = 33\% \pm 5\%$, which could be an indication that the transient flux dip phenomenon is linked to stellar binarity (Henry et al. 2006; Duchêne & Kraus 2013; Winters et al. 2019). This fraction might be even more significant given the selection bias against high-mass-ratio binaries, in which the second star would be too faint to detect a second period.

However, the association between transient flux dips and binarity is not ironclad. First, multiple photometric periods do not necessarily imply binarity. For instance, circumstellar material could exist around single stars at multiple orbital distances and not just at the corotation radius. This could cause eclipses with periods different from the stellar rotation period. Additionally, low-mass, pre-main-sequence stars have been shown to have companion fractions up to twice as high in dispersed clusters, such as Upper Sco and Taurus (Kraus et al. 2008, 2011). A high-resolution imaging survey would be interesting, to determine whether the transient flux dip stars truly have distinct population-level binarity properties relative to other young, low-mass stars.

---

[16] At present, the oldest observed "scallops" are in the Pleiades (Rebull et al. 2016). One of these, EPIC 211013604, might meet the "persistent dip" classification. If so, it is the oldest known.
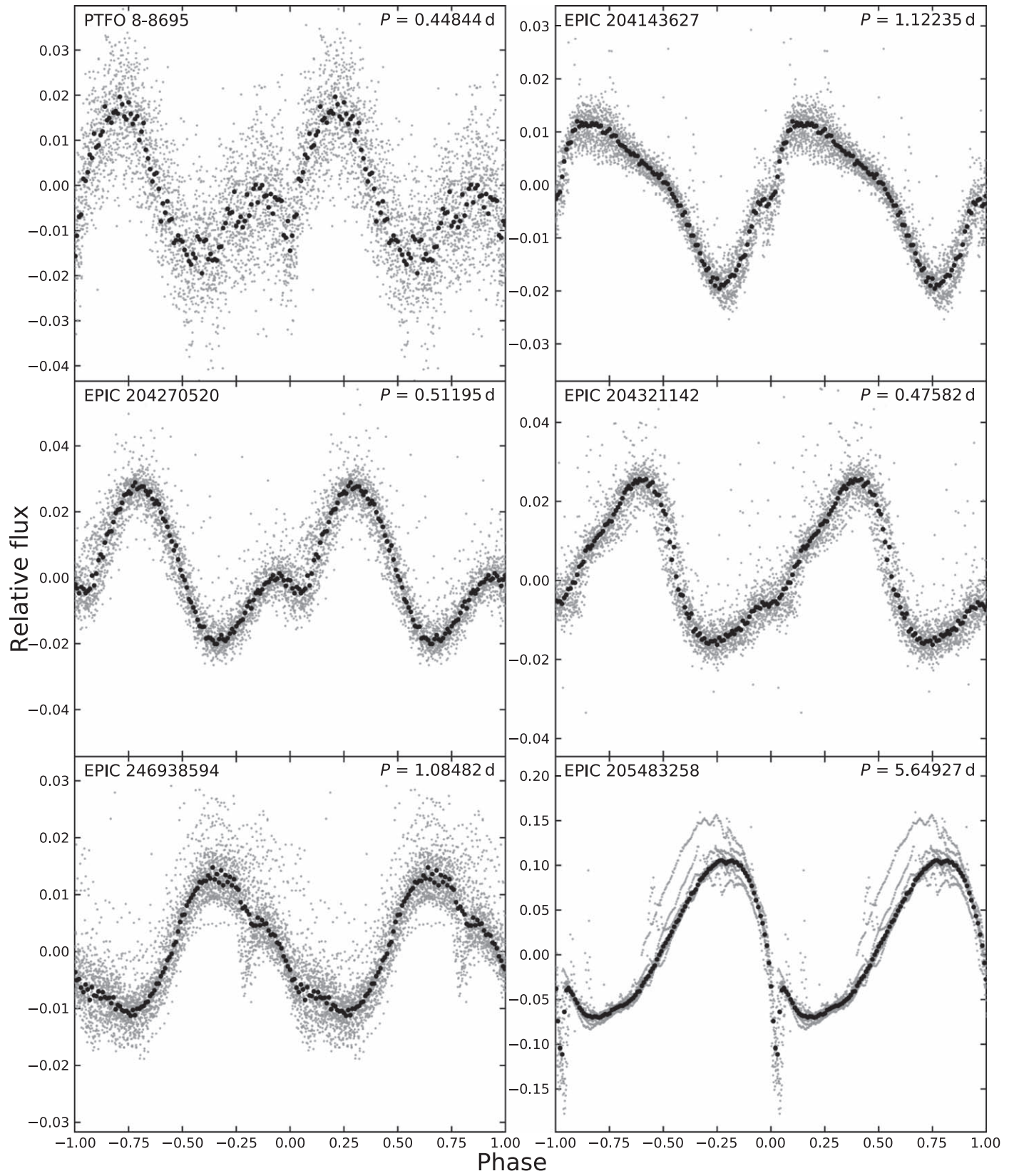
Figure 7. PTFO 8-8695 and its brethren. Shown are the light curves of five transient and persistent flux dip stars, selected based on their similarity to the short-period signal of PTFO 8-8695. The stars are EPIC 204143627, EPIC 204270520, EPIC 204321142, EPIC 246938594, and EPIC 205483258 (RIK-210). RIK-210 has the longest period of any of these objects. All the analogs displayed are either in Taurus or Upper Sco and meet the characteristics of Section 5.3.2. These objects were originally reported by Stauffer et al. (2017), David et al. (2017), and Rebull et al. (2018).

5.4. Physical Interpretation

The evidence for binarity in PTFO 8-8695 is as follows. First, the star is twice as bright as stars of the same color in its kinematic group (Figure 5). Second, it shows two distinct photometric signals. These points alone suggest binarity (Stauffer et al. 2018). For the case of PTFO 8-8695, there is a third line of evidence: the Gaia DR2 entry for PTFO 8-8695 reports a poor fit of the single-star model to the astrometric data. While this could be caused by stellar variability, other cluster members that are just as variable do not typically show the same level of excess astrometric motion. Therefore, the astrometric excess is a suggestive third line of evidence for binarity in PTFO 8-8695. To us, the evidence leads to the conclusion that PTFO 8-8695 is a nearly equal-mass binary consisting of two rapidly rotating stars.

Based on the lack of an infrared excess seen by Yu et al. (2015), the primordial disks of both stars in PTFO 8-8695 seem to have been depleted of hot dust within the inner ∼1 au. This is consistent with the 8.5 ± 1.2 Myr age of the 25 Ori-1 group and the rapid rate at which stars lose their disks between 1 and 10 Myr (e.g., Hernández et al. 2007). The stars are therefore presumably no longer magnetically locked to their disks. This is also suggested by the approximately half-day periodicities of both rotation signals: young disked M dwarfs typically rotate with periods of two days or more due to magnetic locking (e.g., Rebull et al. 2020). If the two stars are within ≈50 au of each other, as required by the NIRC2 adaptive optics imaging, then it would also be expected that the stars would have truncated the outer edges of their respective disks, in a manner seen at the population level in exoplanetary systems (Kraus et al. 2016; Moe & Kratter 2019).

The key question is what causes the transient dips. This is an unsolved problem not only for PTFO 8-8695 but also for the emerging class of similar young and rapidly rotating M dwarfs. Many possible explanations were discussed by Rebull et al. (2016), David et al. (2017), Stauffer et al. (2017), and Zhan et al. (2019). Among the *disfavored* explanations are that the dips are caused by (1) eclipsing binaries, (2) "dipper"-flavor Class I or Class II disks, (3) eclipses of prominences, (4) high-latitude starspots, or (5) dust clouds of particular compositions (Zhan et al. 2019, Figure 10). We also view the possibility of (6) tidally disrupted planetary or cometary material to be implausible, given the synchronicity between dip and rotation periods seen across many systems. Finally, (7) transits of an enshrouded protoplanet can be added to the list of disfavored explanations, based on the chromaticity, asymmetric phase curve, and light-curve changes seen in PTFO 8-8695. The explanations that we view as not yet ruled out include (A) transiting clumps of dust or gas at the Keplerian corotation radius, (B) occultations of hotspots on the stellar surface by an optically thick disk (Zhan et al. 2019), and (C) high-latitude accretion hotspots passing behind the star (Yu et al. 2015). Observations of PTFO 8-8695 over the past decade may offer some hints. PTFO 8-8695's transition between having no dips, one dip, and multiple dips per cycle seems important (Figure 6). The Hα excess observed by Johns-Krull et al. (2016) also seems like an important piece of evidence.

The high-latitude accretion hot-spot scenario seems capable of explaining most of the qualitative characteristics of PTFO 8-8695. Some degree of accretion onto the star seems likely, given the high-velocity (±200 km s^{-1}) components of the observed Hα line profile (Johns-Krull et al. 2016), as well as the Hα equivalent width of 11.4 Å (van Eyken et al. 2012), which is near the boundary separating "classical" and "weak-lined" T Tauri stars (Briceño et al. 2019). The nondetection of any NIR excess could be problematic, but it does not eliminate the possibility that a tenuous amount of dust and gas remains near the star and is able to accrete onto it. The main problem with this explanation is that it seems to require rare circumstances, making it unlikely to be correct for the entire population of transient flux dips. RIK-210 in particular has dips that seem too deep (∼20%) and too asymmetric to be explained by an accretion hot spot (David et al. 2017).

Explanations A and B (circumstellar material at the corotation radius, and occultations of spots by a disk) have the appeal that they are flexible enough to explain not only the transient and persistent-dip stars, but also the "scallop shells" (Stauffer et al. 2017). In the spot occultation scenario (Zhan et al. 2019), the "blobs" that provide the necessary brightness contrast are on the surface of the star, rather than at the corotation radius. The observing geometry would require an inner ring to be projected into a narrow band in front of the stellar disk, in order to produce variations with sufficiently short timescales. The outer disk would also need to either not be present or be misaligned enough and insufficiently flared that it did not obstruct the line of sight to the star. This geometric requirement seems too contrived to occur in even ≲1% of young M dwarf systems.

Thus, while several of the proffered explanations deserve further scrutiny, we consider the clumpy torus of optically thick dust or gas near the corotation radius to be most plausible. The partially ionized circumstellar hydrogen would readily explain the excess Hα emission, and changes in the clumping geometry would lead to changes in the observed eclipse shapes. The long-term stability, punctuated by changes in dip phases, might be understood as an accretion disk subject to strong magnetic fields going through "stalled" states in which material is trapped near corotation (D'Angelo & Spruit 2012). Physical models of this scenario may need to consider such states, in addition to dissociation of the dust population (Millan-Gabet et al. 2007; Dullemond & Monnier 2010). Finally, the question of whether the opacity in fact comes from dust or partially ionized gas (e.g., via gas continuum, atomic lines, or perhaps TiO molecular opacity) remains an additional issue for future exploration.

6. Conclusions

The combination of TESS and Gaia data has clarified a few things about the PTFO 8-8695 system. Our main results are as follows:

1. *The TESS light curve shows two periodic signals.* The "long" signal is a 10% peak-to-peak sinusoid that repeats every 11.98 hr. The "short" signal is a 4% peak-to-peak "dip + asymmetric sinusoid" that repeats every 10.76 hr. The signals beat and therefore cannot be an artifact linked to data processing. Within the angular resolution of the Gaia source catalog, both signals originate from PTFO 8-8695.

2. *The Gaia data imply binarity.* Relative to stars in its kinematic group, PTFO 8-8695 is a photometric binary (Figure 5, top). Relative to stars in its group that are at least as photometrically variable, PTFO 8-8695 also shows signs of astrometric binarity (Figure 5, bottom).

3. *The orbital phase of the dip has changed since the discovery by van Eyken et al. (2012). As shown in Figure 6, the phase seems to have jumped, perhaps twice. This agrees with the recent study by Tanimoto et al. (2020).*

4. *All properties of PTFO 8-8695 are consistent with the emerging class of transient and persistent flux dip stars. Analog light curves are shown in Figure 7. Properties of this variability class are enumerated in Section 5.3.2.*

The physical mechanism that explains the transient and persistent flux dips is unresolved. Our preferred explanation is that a clumpy torus of dust or gas is near the Keplerian corotation radius and periodically occults the star. The chromaticity, out-of-eclipse variability, and jumping orbital phase of PTFO 8-8695 all disfavor the explanation of an enshrouded, transiting protoplanet. Though PTFO 8-8695 may not be a planet, understanding it and its analogs is a worthy problem that seems likely to provide insight into how gas and dust disperse from young protostellar disks. Understanding this process would, in turn, teach us about the birth environments of the majority of habitable-zone Earth-sized planets (Dressing & Charbonneau 2013).

When this manuscript was at an advanced stage, we received notice of a paper by Koen (2020) that was in press at the *Monthly Notices* before submission of our manuscript. Our studies independently reached the same conclusions: the TESS light curve shows two periodic signals, and the properties of PTFO 8-8695 are consistent with the emerging class of transient and persistent flux dip stars. Koen (2020) reached these conclusions by modeling the TESS light curve as a truncated sum of Fourier terms and concluded that the two signals are most simply interpreted as coming from two stars. Our analysis of the Gaia data provides independent support for the conclusion that PTFO 8-8695 is a binary. We also note the agreement between the TESS dip ephemeris and that from Tanimoto et al. (2020).

Software: astrobase (Bhatti et al. 2018), astropy (Astropy Collaboration et al. 2018), astroquery (Ginsburg et al. 2018), cdips-pipeline (Bhatti et al. 2019), corner (Foreman-Mackey 2016), exoplanet (Agol et al. 2019), exoplanet (Foreman-Mackey et al. 2020), and its dependencies (Kipping 2013; Theano Development Team 2016; Agol et al. 2019; Luger et al. 2019), IPython (Pérez & Granger 2007), lightkurve (Lightkurve Collaboration et al. 2018), matplotlib (Hunter 2007), MESA (Paxton et al. 2011, 2013, 2015), numpy (Walt et al. 2011), pandas (McKinney 2010), pyGAM (Servén et al. 2018), PyMC3 (Salvatier et al. 2016), scipy (Jones et al. 2001), SPOC R4.0 (Jenkins et al. 2016), tesscut (Brasseur et al. 2019), wotan (Hippke et al. 2019).

Facilities: Astrometry: Gaia (Gaia Collaboration et al. 2016, 2018). *Imaging*: Second Generation Digitized Sky Survey, Keck:II (NIRC2; www2.keck.hawaii.edu/inst/nirc2). *Spectroscopy*: Keck:I (HIRES; Vogt et al. 1994). *Photometry*: TESS (Ricker et al. 2015).

ORCID iDs

L. G. Bouma https://orcid.org/0000-0002-0514-5538
J. N. Winn https://orcid.org/0000-0002-4265-047X
G. R. Ricker https://orcid.org/0000-0003-2058-6662
R. Vanderspek https://orcid.org/0000-0001-6763-6562
D. W. Latham https://orcid.org/0000-0001-9911-7388
S. Seager https://orcid.org/0000-0002-6892-6948
J. M. Jenkins https://orcid.org/0000-0002-4715-9460
T. Barclay https://orcid.org/0000-0001-7139-2724
K. A. Collins https://orcid.org/0000-0001-6588-9574
D. R. Louie https://orcid.org/0000-0002-2457-272X
S. N. Quinn https://orcid.org/0000-0002-8964-8377
M. E. Rose https://orcid.org/0000-0003-4724-745X
J. C. Smith https://orcid.org/0000-0002-6148-7903
B. Wohler https://orcid.org/0000-0002-5402-9613

References   Q2

Agol, E., Luger, R., & Foreman-Mackey, D. 2019, arXiv:1908.03222
Ansdell, M., Gaidos, E., Rappaport, S. A., et al. 2016, ApJ, 816, 69
Astropy Collaboration, Price-Whelan, A. M., Sipőcz, B. M., et al. 2018, AJ, 156, 123
Barnes, J. W., van Eyken, J. C., Jackson, B. K., Ciardi, D. R., & Fortney, J. J. 2013, ApJ, 774, 53
Belokurov, V., Penoyre, Z., Oh, S., et al. 2020, arXiv:2003.05467
Bhatti, W., Bouma, L., & Yee, S. 2019, cdips-pipeline, v0.1.0, Zenodo, doi:10.5281/zenodo.3370324
Bhatti, W., Bouma, L. G., & Wallace, J. 2018, astrobase, Zenodo, doi:10.5281/zenodo.1469822   Q4
Blanton, M. R., Bershady, M. A., Abolfathi, B., et al. 2017, AJ, 154, 28
Bodman, E. H. L., Quillen, A. C., Ansdell, M., et al. 2017, MNRAS, 470, 202
Bouma, L. G., Hartman, J. D., Bhatti, W., Winn, J. N., & Bakos, G. Á 2019, ApJS, 245, 13
Brasseur, C. E., Phillip, C., Fleming, S. W., Mullally, S. E., & White, R. L. 2019, Astrophysics Source Code Library, ascl:1905.007   Q5
Briceño, C., Calvet, N., Hernández, J., et al. 2005, AJ, 129, 907
Briceño, C., Calvet, N., Hernández, J., et al. 2019, AJ, 157, 85
Briceño, C., Hartmann, L., Hernández, J., et al. 2007a, ApJ, 661, 1119
Briceño, C., Preibisch, T., Sherry, W. H., et al. 2007b, Protostars and Planets V, 345   Q6
Bryson, S. T., Jenkins, J. M., Klaus, T. C., et al. 2020, Kepler Data Processing Handbook: Target and Aperture Definitions: Selecting Pixels for Kepler Downlink, Kepler Data Processing Handbook (KSCI-19081-003)
Burnham, K. P., & Anderson, D. R. 2016, Sociological Methods & Research   Q7
Ciardi, D. R., Eyken, J. C. v., Barnes, J. W., et al. 2015, ApJ, 809, 42
Cody, A. M., & Hillenbrand, L. A. 2018, AJ, 156, 71
Cottle, J., Covey, K. R., Suárez, G., et al. 2018, ApJS, 236, 27
Cropper, M., Katz, M., Sartoretti, D., et al. 2018, A&A, 616, A5
D'Angelo, C. R., & Spruit, H. C. 2012, MNRAS, 420, 416
David, T. J., Petigura, E. A., Hillenbrand, L. A., et al. 2017, ApJ, 835, 168
Donati, J. F., Moutou, C., Malo, L., et al. 2016, Natur, Advance Online Publication
Donati, J.-F., Yu, L., Moutou, C., et al. 2017, MNRAS, 465, 3343
Dressing, C. D., & Charbonneau, D. 2013, ApJ, 767, 95
Duchêne, G., & Kraus, A. 2013, ARA&A, 51, 269
Dullemond, C. P., & Monnier, J. D. 2010, ARA&A, 48, 205
Evans, D. W., Riello, M., De Angeli, F., et al. 2018, A&A, 616, A4
Fang, M., van Boekel, R., Wang, W., et al. 2009, A&A, 504, 461
Foreman-Mackey, D. 2016, JOSS, 24

Q8 Foreman-Mackey, D., Czekala, I., Luger, R., et al. 2020, exoplanet-dev/
        exoplanet v0.2.6
    Gaia Collaboration, Brown, A. G. A., Vallenari, A., et al. 2018, A&A, 616, A1
    Gaia Collaboration, Prusti, T., de Bruijne, J. H. J., et al. 2016, A&A, 595, A1
    Gelman, A., & Rubin, D. B. 1992, StaSc, 7, 457
    Ginsburg, A., Sipocz, B., Parikh, M., et al. 2018, Astropy/Astroquery: V0.3.7
        Release
    Gunn, J. E., Siegmund, W. A., Mannery, E. J., et al. 2006, AJ, 131, 2332
    Henry, T. J., Jao, W.-C., Subasavage, J. P., et al. 2006, AJ, 132, 2360
    Hernández, J., Calvet, N., Briceño, C., et al. 2007, ApJ, 671, 1784
    Hippke, M., David, T. J., Mulders, G. D., & Heller, R. 2019, arXiv:1906.00966
    Hoffman, M. D., & Gelman, A. 2014, Journal of Machine Learning Research,
        15, 1593
    Howarth, I. D. 2016, MNRAS, 457, 3769
    Howell, S. B., Sobeck, C., Haas, M., et al. 2014, PASP, 126, 398
    Hunter, J. D. 2007, CSE, 9, 90
    Jeffries, R. D., Maxted, P. F. L., Oliveira, J. M., & Naylor, T. 2006, MNRAS,
        371, L6
    Jenkins, J. M., Twicken, J. D., McCauliff, S., et al. 2016, Proc. SPIE, 9913,
        99133E
    Johns-Krull, C. M., Prato, L., McLane, J. N., et al. 2016, ApJ, 830, 15
    Jones, E., Oliphant, T., Peterson, P., et al. 2001, Open Source Scientific Tools
        for Python
    Kamiaka, S., Masuda, K., Xue, Y., et al. 2015, PASJ, 67, 94
    Kipping, D. M. 2013, MNRAS, 435, 2152
    Koen, C. 2015, MNRAS, 450, 3991
    Koen, C. 2020, MNRAS
    Kounkel, M., Covey, K., Suárez, G., et al. 2018, AJ, 156, 84
    Kraus, A. L., Ireland, M. J., Huber, D., Mann, A. W., & Dupuy, T. J. 2016, AJ,
        152, 8
    Kraus, A. L., Ireland, M. J., Martinache, F., & Hillenbrand, L. A. 2011, ApJ,
        731, 8
    Kraus, A. L., Ireland, M. J., Martinache, F., & Lloyd, J. P. 2008, ApJ, 679, 762
    Lee, C.-H., & Chiang, P.-S. 2018, ApJL, 852, L24
    Lightkurve Collaboration, Cardoso, J. V. d. M., Hedges, C., et al. 2018,
        Lightkurve: Kepler and TESS time series analysis in Python, Astrophysics
        Source Code Library, ascl:1812.013
    Lindegren, L., Hernández, J., Bombrun, A., et al. 2018, A&A, 616, A2
    Lomb, N. R. 1976, Ap&SS, 39, 447
    Luger, R., Agol, E., Foreman-Mackey, D., et al. 2019, AJ, 157, 64
    Luger, R., Agol, E., Kruse, E., et al. 2016, AJ, 152, 100
    Luger, R., Kruse, E., Foreman-Mackey, D., Agol, E., & Saunders, N. 2018, AJ,
        156, 99
    Majewski, S. R., Schiavon, R. P., Frinchaboy, P. M., et al. 2017, AJ, 154, 94
    Maucó, K., Briceño, C., Calvet, N., et al. 2018, ApJ, 859, 1
Q9 McKinney, W. 2010, in Proc. 9th Python in Science Conf., ed.
        S. van der Walt & J. Millman, 51

    Millan-Gabet, R., Malbet, F., Akeson, R., et al. 2007, Protostars and Planets
        V, 539
    Moe, M., & Kratter, K. M. 2019, arXiv:1912.01699
    Onitsuka, M., Fukui, A., Narita, N., et al. 2017, PASJ, 69
    Parks, J. R., Plavchan, P., White, R. J., & Gee, A. H. 2014, ApJS, 211, 3
    Paxton, B., Bildsten, L., Dotter, A., et al. 2011, ApJS, 192, 3
    Paxton, B., Cantiello, M., Arras, P., et al. 2013, ApJS, 208, 4
    Paxton, B., Marchant, P., Schwab, J., et al. 2015, ApJS, 220, 15
    Pérez, F., & Granger, B. E. 2007, CSE, 9, 21
    Raetz, S., Schmidt, T. O. B., Czesla, S., et al. 2016, MNRAS, 460, 2834
    Rebull, L. M., Stauffer, J. R., Bouvier, J., et al. 2016, AJ, 152, 114
    Rebull, L. M., Stauffer, J. R., Cody, A. M., et al. 2018, AJ, 155, 196
    Rebull, L. M., Stauffer, J. R., Cody, A. M., et al. 2020
    Ricker, G. R., Winn, J. N., Vanderspek, R., et al. 2015, JATIS, 1, 014003
    Rizzuto, A. C., Vanderburg, A., Mann, A. W., et al. 2018, arXiv:1808.07068
    Salvatier, J., Wieckiâ, T. V., & Fonnesbeck, C. 2016, PyMC3: Python
        Probabilistic Programming Framework
    Scargle, J. D. 1982, ApJ, 263, 835
    Schmidt, T. O. B., Neuhäuser, R., Briceño, C., et al. 2016, A&A, 593, A75
    Servén, D., Brummitt, C., & Abedi, H. 2018, dswah/pyGAM: v0.8.0
    Shporer, A. 2017, PASP, 129, 072001
    Smith, J. C., Stumpe, M. C., Cleve, J. E. V., et al. 2012, PASP, 124, 1000
    Stassun, K. G., Oelkers, R. J., Paegert, M., et al. 2019, arXiv:1905.10694
    Stassun, K. G., Oelkers, R. J., Pepper, J., et al. 2018, AJ, 156, 102
    Stauffer, J., Cameron, A. C., Jardine, M., et al. 2017, AJ, 153, 152
    Stauffer, J., Cody, A. M., McGinnis, P., et al. 2015, AJ, 149, 130
    Stauffer, J., Rebull, L. M., Cody, A. M., et al. 2018, AJ, 156, 275
    Stumpe, M. C., Smith, J. C., Catanzarite, J. H., et al. 2014, PASP, 126, 100
    Tanimoto, Y., Yamashita, T., Ui, T., et al. 2020, PASJ, arXiv:2001.
        00148 [astro-ph.EP]
    Tenenbaum, P., & Jenkins, J. 2018, TESS Science Data Products Description
        Document, EXP-TESS-ARC-ICD-0014 Rev D, https://archive.stsci.edu/
        missions/tess/doc/EXP-TESS-ARC-ICD-TM-0014.pdf
    Theano Development Team 2016, arXiv:1605.02688
    van Eyken, J. C., Ciardi, D. R., von Braun, K., et al. 2012, ApJ, 755, 42
    VanderPlas, J. T., & Ivezić, Z. 2015, ApJ, 812, 18
    Vogt, S. S., Allen, S. L., Bigelow, B. C., et al. 1994, Proc. SPIE, 2198
    Walt, S. v. d., Colbert, S. C., & Varoquaux, G. 2011, CSE, 13, 22
    Winn, J. N. 2010, in Exoplanet Transits and Occultations, ed. S. Seager, 55
    Winters, J. G., Henry, T. J., Jao, W.-C., et al. 2019, AJ, 157, 216
    Wright, E. L., Eisenhardt, P. R. M., Mainzer, A. K., et al. 2010, AJ, 140,
        1868
    Yu, L., Donati, J.-F., Hébrard, E. M., et al. 2017, MNRAS, 467, 1342
    Yu, L., Winn, J. N., Gillon, M., et al. 2015, ApJ, 812, 48
    Zasowski, G., Cohen, R. E., Chojnowski, S. D., et al. 2017, AJ, 154, 198
    Zhan, Z., Günther, M. N., Rappaport, S., et al. 2019, ApJ, 876, 127
    Ziegler, C., Law, N. M., Baranec, C., et al. 2018, arXiv:1806.10142